

This is an Open Access document downloaded from ORCA, Cardiff University's institutional repository: <https://orca.cardiff.ac.uk/id/eprint/145135/>

This is the author's version of a work that was submitted to / accepted for publication.

Citation for final published version:

Alli, Uthman, McCarthy, Kieran, Baragau, Ioan-Alexandru, Power, Nicholas P., Morgan, David J., Dunn, Steven, Killian, Seamus, Kennedy, Tadhg and Kellici, Suela 2022. In-situ continuous hydrothermal synthesis of TiO<sub>2</sub> nanoparticles on conductive N-doped MXene nanosheets for binder-free li-ion battery anodes. *Chemical Engineering Journal* 430 (4), 132976. 10.1016/j.cej.2021.132976

Publishers page: <http://dx.doi.org/10.1016/j.cej.2021.132976>

Please note:

Changes made as a result of publishing processes such as copy-editing, formatting and page numbers may not be reflected in this version. For the definitive version of this publication, please refer to the published source. You are advised to consult the publisher's version if you wish to cite this paper.

This version is being made available in accordance with publisher policies. See <http://orca.cf.ac.uk/policies.html> for usage policies. Copyright and moral rights for publications made available in ORCA are retained by the copyright holders.



# In-situ Continuous Hydrothermal Synthesis of TiO<sub>2</sub> Nanoparticles on Conductive N-doped MXene Nanosheets for Binder-Free Li-ion Battery Anodes

Uthman Alli,<sup>a</sup> Kieran McCarthy,<sup>b,c</sup> Ioan-Alexandru Baragau,<sup>a,f</sup> Nicholas P. Power,<sup>d</sup> David J. Morgan,<sup>e</sup> Steven Dunn,<sup>a</sup> Seamus Killian,<sup>b,c</sup> Tadhg Kennedy,<sup>\*b,c</sup> and Suela Kellici<sup>\*a</sup>

<sup>a</sup>School of Engineering, London South Bank University, 103 Borough Road, London, SE1 0AA, United Kingdom. Website: [www.nano2d.co.uk](http://www.nano2d.co.uk); E-Mail: [kellicis@lsbu.ac.uk](mailto:kellicis@lsbu.ac.uk)

<sup>b</sup>Department of Chemical Sciences, University of Limerick, V94 T9PX, Limerick, Ireland

<sup>c</sup>Bernal Institute, University of Limerick, V94 T9PX, Limerick, Ireland, [tadhg.kennedy@ul.ie](mailto:tadhg.kennedy@ul.ie)

<sup>d</sup>School of Life Health & Chemical Sciences, Open University, Walton Hall, Milton Keynes, MK7 6AA, United Kingdom

<sup>e</sup>Cardiff Catalysis Institute, School of Chemistry, Cardiff University, Park Place, Cardiff, CF10 3AT, United Kingdom

<sup>f</sup>National Institute of Materials Physics, Atomistilor 405A, 077125, Magurele, Ilfov, Romania

## Abstract

Anode materials are key to determining the energy density, cyclability and of life recyclability for Li-ion energy storage systems. High surface area materials, such as MXenes, can be manufactured with improved electrochemical properties that remove the need for polymeric binders or hazardous chemicals that pose a challenge to recycle Li-ion batteries. However, there remains a challenge to produce Li-ion anode materials that are binder free and poses energy storage characteristics that match the current carbon-based electrodes. Here we show the synthesis of N-doped MXene-TiO<sub>2</sub> hybrid anode materials using an aqueous route. N-doped TiO<sub>2</sub>-MXene was modified using a single step continuous hydrothermal process. Capacity tests indicate an improvement from the initial specific energy capacity of 305 mAhg<sup>-1</sup> to 369 mAhg<sup>-1</sup> after 100 cycles at a charge rate of 0.1 C and a Coulombic

efficiency of 99.7%. This compares to  $252 \text{ mAhg}^{-1}$  for the unmodified MXene which exhibited significant capacity fade to  $140 \text{ mAhg}^{-1}$ . The ability to manufacture a Li-ion anode that does not require toxic chemicals for processing into an electrode and exhibits good energy storage characteristics in a binder free system is a significant step forward for energy storage applications.

**Keywords:** MXene; nitrogen-doping; continuous hydrothermal flow synthesis; binder-free electrode processing.

## 1. Introduction

Lithium-ion batteries (LIBs) are energy storage devices that have emerged as the dominant current battery technology due to their high energy density and excellent cycling performance[1,2]. Lithium has low molecular weight and density and is highly suitable for intercalating into layered materials, thereby showing high volumetric energy density. Despite these exciting properties exhibited by LIBs, they are limited by power performance, costs, safety and environmental concerns from toxicity of its components and lithium mining.

LIBs store energy by transporting lithium ions from the cathode to the anode during the charging process and vice-versa during the discharge process. A typical LIB comprises of three components; the anode (usually graphite), the cathode (typically lithium metal oxides, e.g.,  $\text{LiCoO}_2$ ), and an electrolyte (non-aqueous) that allows for reversible lithiation and delithiation over a wide potential range. Lithium metal oxides (LMOs) as cathode materials offer high chemical potential (vs  $\text{L/Li}^+$ ), while graphite as an anode material is naturally abundant, low cost, and has a layered structure suitable for intercalation[3,4]. Despite the long cycle lives shown by LIBs, one major disadvantage is the use of standard polymeric binders in electrode fabrication. An example is poly vinylidene difluoride (PVDF), a poly-fluoroalkyl (PFA) compound classified as a "forever chemical" due to its longevity in the

environment. A potential solution that eradicates the use of forever chemical is the aqueous processing of MXenes into a stable colloidal suspension due to its negatively charged nanosheets. Previous reports on the use of MXenes as Li-ion anodes show a potential means to eliminate environmentally unfriendly polymeric binders from LIB electrodes[5–7].

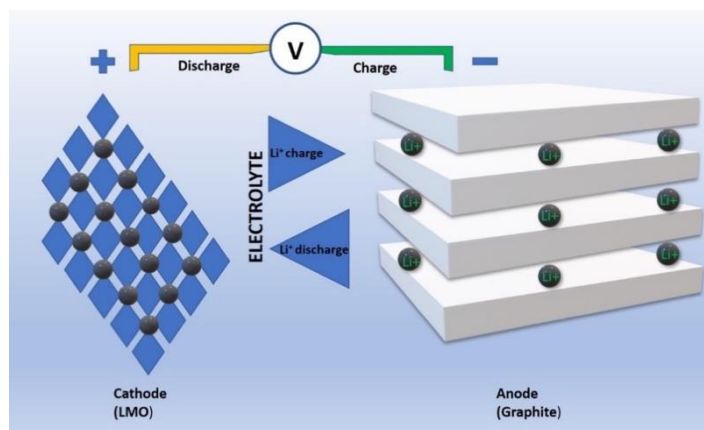


**Fig. 1** Schematic of Lithium-ion battery energy storage process

Also, electrode fabrication in LIBs requires the use of N-methyl-2-pyrrolidone (NMP), a toxic solvent in slurry processing the electrodes[8–11]. These negatively impacts both the environmental friendliness and cost of battery manufacturing currently. To overcome this, the solution is MXene, which enables aqueous processing due to its excellent hydrophilic surface. This eliminates the use of toxic electrode processing solvents[12]. In addition, MXenes have high electronic conductivity ( $6500 \text{ S cm}^{-1}$ ), enabling them to serve as an active material and a current collector[13,14].

MXenes are transitional metal carbides, nitrides, and carbonitrides that exhibit ultrahigh electronic conductivity and excellent charge storage properties[13,15]. MXenes were first reported by Gogotsi et al. in 2011, highlighting its synthesis from MAX phase precursor by a selective acid etching process[15]. In the MXene synthesis process, hydrofluoric acid (HF) selectively etch out the "A" element to produce MXenes with a general formula  $M_{n+1}X_nT_x$ , where  $n= 1,2, \text{ or } 3$ , and  $T_x$  are surface terminations such as O, OH, and F. Examples of

MXenes include  $\text{Ti}_3\text{C}_2\text{T}_x$ ,  $\text{Ti}_2\text{CT}_x$ ,  $\text{Ti}_3\text{CNT}_x$ ,  $\text{Nb}_4\text{C}_3\text{T}_x$ , etc.[13,15]. Reversible redox reactions occurring at the titanium surface (Ti) in MXene provide a pseudo-capacitance, thereby increasing the faradaic performance of a MXene electrode[16]. A tapped density of  $4 \text{ g cm}^{-3}$  exhibited by MXenes reduces the electrode's mass loading compared to 2D graphene ( $0.4 \text{ g cm}^{-3}$ ). A reported high volumetric capacitance of up to  $900 \text{ F cm}^{-3}$  in MXene attracts increasing interest in energy storage applications[13,14]. However, the stability of MXenes in an aqueous solution, re-stacking of its nanosheets, and limited control of its surface functionalities limit the full use of its properties. A potential solution is through the surface and chemical functionalisation of 2D MXenes with metal oxides such as titanium (iv) oxide ( $\text{TiO}_2$ ) or doping with heteroatoms such as nitrogen[17]. The growth of  $\text{TiO}_2$  nanoparticles between MXene sheets prevents re-stacking, thereby keeping sheets separated. During the doping process, the dopant (nitrogen) behaves like an electron donor. It replaces carbon in the crystal lattice of the semiconducting material by generating an extra valence electron in modulating the conductivity of the semiconductor material.

Due to its natural abundance, low cost, high safety and non-toxic nature[18],  $\text{TiO}_2$  serves as an attractive Li-ion anode material in energy storage[19,20] and various applications such as photocatalysis[21–23] and water treatment[21,23].  $\text{TiO}_2$  also exhibits a low volume expansion (<4%) during the lithiation process, a prerequisite for long cycle life materials[24–26]. However, challenges exist in performance, chiefly related to the poor electrical conductivity and sluggish Li-ion diffusion within the material[27,28]. Utilising nano- $\text{TiO}_2$  is a potential route to overcome this due to improved surface area and reduced diffusion distance for Li-ion transport compared to bulk materials[29]. Furthermore, combining  $\text{TiO}_2$  nanoparticles with highly conductive 2D materials such as MXenes has the potential to boost performance significantly while simultaneously eliminating the need for conventional fluorinated polymeric binders[26].

Advanced surface modifications of 2D materials via a unique route of synthesis offer an advantage of distinct morphologies, improved surface area and surface functionalities. In addition, these modifications alter the material structure by size tuning and engineering defects in the material, thereby causing a change in the electronic and optoelectronic properties[30]. As stand-alone materials do not have enough properties to render practical functions, it is advantageous to combine the properties and modified functionalities of 2D MXenes and TiO<sub>2</sub> nanoparticles as electrode materials to enhance electrochemical performance. However, the current approaches in the synthesis of materials face challenges, including toxic precursors, non-uniformity of particle size distribution, lengthy manufacturing time, and energy costs. As a result, there is a need to adopt synthetic strategies that overcome these challenges by providing a rapid, clean and scalable material synthesis process while delivering high-performance materials.

Continuous Hydrothermal Flow Synthesis (CHFS) is employed here as a favourable methodology that offers a single-step process of delivering water-soluble precursors with a flow of supercritical water at 374 °C and 22.4 MPa for homogeneously producing highly crystalline nanostructures[30–32]. This method exploits the properties of supercritical water, such as its reduced dielectric constant and increased dissociation to H<sup>+</sup> and OH<sup>-</sup> ions which facilitate the rapid synthesis of various metal oxides through hydrolyses, dehydration, and precipitation[33]. CHFS methodology delivers fine particles, single crystals, and metal oxides by controlling the reaction medium's viscosity, density, and dielectric constant through changes in the reaction temperature and pressure. This hands-on approach offers control over the particle size, morphology, and crystal structure of as-synthesised materials[14,32–35]. Compared to traditional methods, CHFS saves time (within a fraction of a second) and energy in delivering quality and reproducible homogenous

materials[32,36–39]. In addition, the CHFS process has a low environmental impact, as shown in the synthesis of graphene quantum dots.

## 2. Experimental Section

Chemicals: MAX phase  $\text{Ti}_2\text{AlC}$  (Maxthal 211) was purchased from Kanthal AB<sup>®</sup> 211. 40% hydrofluoric acid (HF), 99% potassium carbonate and anhydrous 99.9% dimethyl sulfoxide (DMSO) were purchased from Sigma Aldrich (UK). 32% ammonia was purchased from Fisher Scientific (UK). All chemicals were used as received without any further purification. 15 M $\Omega$  deionised (DI) water obtained from an ELGA Pure Lab system was used.

### 2.1 MXene Synthesis

$\text{Ti}_2\text{C}$  MXene was prepared following processes described in the literature by Gogotsi and co-workers[15].  $\text{Ti}_2\text{AlC}$  MAX phase material (6 g) was added slowly into 20% HF (200 mL) in a large flask. The resulting mixture was stirred mildly at room temperature for 24 h. Solid materials were obtained by vacuum filtration of the slurry and washed with DI water (2 L) until a pH of 6. Wet solids were collected and freeze-dried to obtain multilayered MXene powder (*m*-MXene). *m*-MXene was further delaminated into fewer layers by bath sonication in DMSO for 24 hrs and centrifuged at 3500 rpm for 20 minutes to obtain delaminated MXenes (*d*-MXenes). The delaminated MXene was used as starting precursor in the hydrothermal treatment process and referred to as “untreated MXene”.

## 2.2 Continuous Hydrothermal Flow Synthesis (CHFS) of N-doped MXene-TiO<sub>2</sub> hybrids

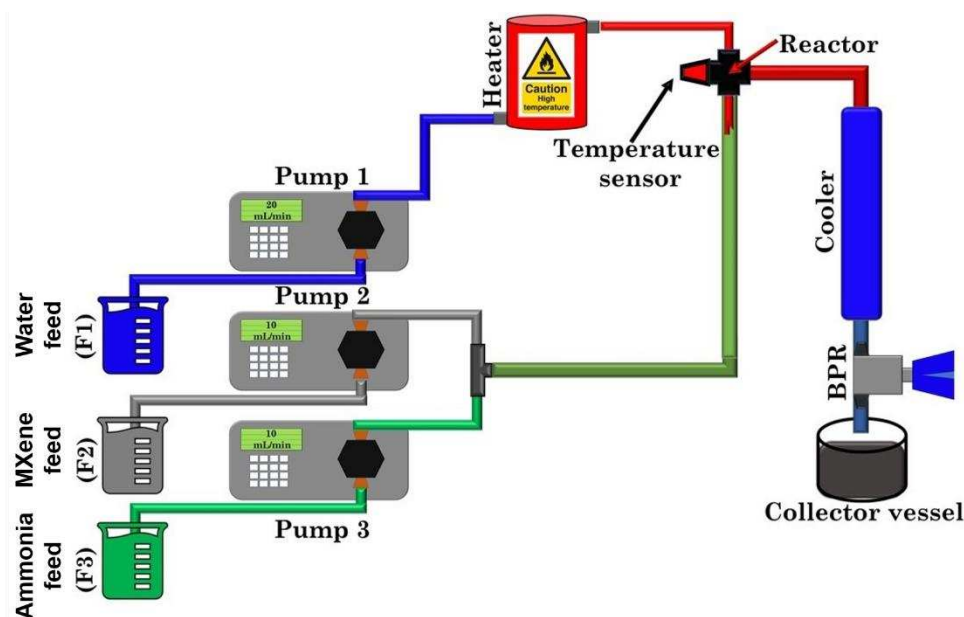


**Fig. 2** Schematic of continuous hydrothermal flow synthesis of N-doped MXene-TiO<sub>2</sub> hybrids consisting of three feeds delivering superheated water ( $T = 350\text{ }^{\circ}\text{C}$  or  $T = 450\text{ }^{\circ}\text{C}$ ;  $P = 22.4\text{ MPa}$ ), MXene (which also served as TiO<sub>2</sub> precursor) and ammonia (N-source) precursors. BPR = back-pressure regulator.

Using the CHFS schematic in **Fig. 2**, CHFS experiments were conducted to synthesise N-doped MXene/TiO<sub>2</sub> composites at different temperatures ( $350\text{ }^{\circ}\text{C}$  or  $450\text{ }^{\circ}\text{C}$ ). The system consists of three pumps F1, F2, and F3, as labelled in **Fig. 2**, delivering aqueous mixtures of de-ionised (DI) water in F1, 2 mg/mL delaminated MXene solution in F2, and 0.5 M ammonia in F3 at a flow rate of  $20\text{ mL min}^{-1}$ ,  $5\text{ mL min}^{-1}$  and  $5\text{ mL min}^{-1}$  in pumps F1, F2 and F3 respectively. This aqueous mixture of MXene in P2 was pumped to meet a flow of aqueous ammonia in F3 at a T-junction. This mixture then meets superheated water ( $T = 350\text{ }^{\circ}\text{C}$  and  $450\text{ }^{\circ}\text{C}$ ,  $P = 22.4\text{ MPa}$ ) from F1 at the mixing point R, where product formation occurs continuously. Experimental CHFS operating conditions (pressure and flow rate) remained the same for the different temperature reactions. The reaction temperature was

monitored by a K-type thermocouple connected to the 1/4-inch Swagelok cross union stainless steel mixing point to read the temperature data on a Pico log software. The resulting suspension was cooled by passing through a vertical cooler, and the slurry was collected from the tubing outlet of the back-pressure regulator (BPR). The assembled products were centrifuged and washed several times to a pH of 6. The precipitate was freeze-dried for 24 hrs, and solid particles were collected for characterisation. The as-synthesised materials at two different temperatures of 350°C and 450°C were labelled as NMT350 and NMT450, respectively.

### 2.3 Equipment and Techniques

Samples were freeze-dried using a Heto Powder Dry PL3000 device. Slurries were frozen with liquid nitrogen and dried for 24 hrs. Scanning Electron Microscopy imaging (SEM) was acquired using a Zeiss Upra 55VP field emission gun scanning electron microscope. Powdered samples were prepared by sputter coating of gold to ensure conduction of the layer. Samples were imaged at 5 kV with secondary electron imaging (SEI). Transmission Electron Microscopy imaging (TEM) was acquired for particle size determination and morphology analysis using a JEOL JEM-1400 microscope with an accelerating voltage of 80 kV. Samples were prepared on copper grids (Holey Carbon Film, 300 mesh Cu, Agar Scientific, UK) by dispensing a small amount in ethanol and adding a few drops of the suspension over the TEM grids. Particle size measurements were performed with ImageJ particle size analysis software. X-ray photoelectron spectroscopy (XPS) measurements were performed using a Thermo Fisher Scientific K-alpha<sup>+</sup> spectrometer utilising a micro-focused monochromatic Al X-ray source operating at 72 W (6 mA x 12 kV) and with the 400-micron spot mode, which averages over an elliptical area of approximately 400 x 600 microns. Data was recorded at pass energies of 150 eV for survey scans and 40 eV for a high-resolution scan with 1 eV and 0.1 eV step sizes. The charge neutralisation of the

sample was achieved using a combination of both low-energy electrons and argon ions. Data analysis was performed using CasaXPS (v2.3.24) using Scofield sensitivity factors and an electron escape depth dependence of -0.6 after subtraction of a Shirley-type background. Raman spectroscopy measurements were performed on a Jobin Yvon Labram HR laser Raman microprobe equipped with a 473 nm laser to investigate the composition of the samples. A Bruker D8 ADVANCE X-ray diffractometer equipped with a ceramic copper target X-ray tube was used to obtain the XRD patterns. The Rietveld refinement of powder diffraction data was conducted using Match software (Crystal Impact) equipped with Fullprof program.

Electrochemical investigations were conducted using a two-electrode Swagelok-type cell consisting of Cu foil current collectors. The N-MXene/TiO<sub>2</sub> nanocomposite served as the active material acted of the working electrode with Li foil as the counter and reference electrodes. A Celgard separator (2400) was used and saturated with a carbonate-based electrolyte solution of 1M LiPF<sub>6</sub> [EC/DMC 1:1]. HCs were tested over the voltage window 0 – 3 V using a Biologic MPG-2 for all galvanostatic measurements.

## 2.4 Electrode Fabrication

The N-doped MXene/TiO<sub>2</sub> nanocomposite was mixed with de-ionised water in a ratio of 1:10 w/v and stirred for 12 hrs to form a homogenous and viscous slurry. The slurry was coated onto a Cu foil substrate (of thickness 9  $\mu$ m) using a laboratory-scale doctor blade machine, without any binders or conductive additives. The MXene tape was air-dried for 24 h, and further vacuum-dried at 110 °C for 60 minutes to ensure all water was removed. Samples were cut with a square punch to an area of 0.5 cm<sup>2</sup> and an average mass loading of 0.3 mg/cm<sup>2</sup>.

### 3. Results and Discussion

We have explored a rapid synthesis approach that delivers MXene (which also functioned as  $\text{TiO}_2$  precursor) and ammonia (N-source) continuously into a supercritical environment in synthesising N-doped MXenes decorated with  $\text{TiO}_2$  nanoparticles.  $\text{TiO}_2$  nanoparticles have been produced in situ through a one-step hydrothermal process from MXene as a starting precursor. MXene (containing Ti atoms) is controllably oxidised during the hydrothermal method and form  $\text{TiO}_2$  on the edges of the MXene sheets, and the surface defects are produced after the etching process. As the hydrothermal process proceeds, the nucleus of the  $\text{TiO}_2$  particles grows due to the diffusion of Ti atoms from the MXene surface. Ti-C bonds are broken during this process, C-C bonds are formed, and an anticipated  $\text{CO}_2$  is released during the reaction process as supported by precedence from literature[40]. A combination of all these processes results in the formation of  $\text{TiO}_2$  nanoparticles on the surface of N-doped MXene sheets. Characteristically, this is also associated with the formation of carbon. The as-synthesised materials were collected and characterised for various analyses.

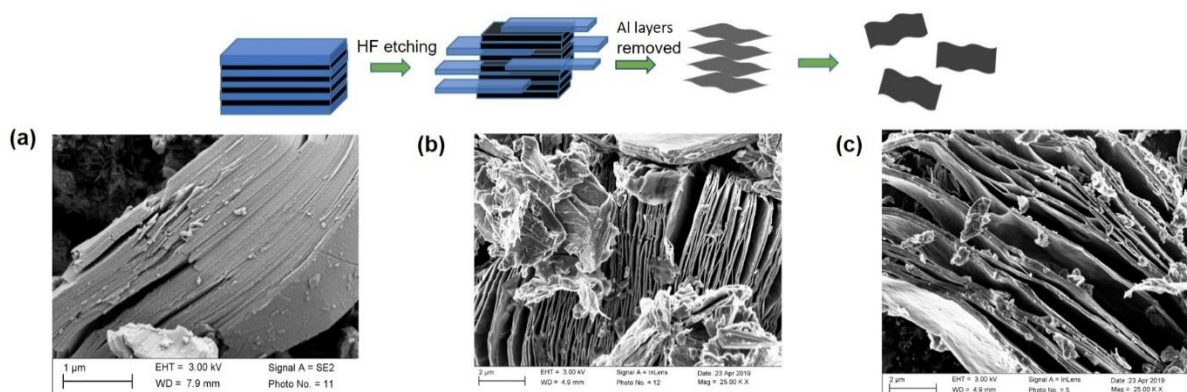


**Fig. 3** SEM Images of (a) MAX phase material (b) HF treated MXene (*m*-MXene) (c) ultrasonicated MXene (labelled as *d*-MXene or untreated MXene). This delaminated MXene was used as starting precursor in the CHFS treatment process.

Electron microscopy analyses were used to investigate the effect of the continuous hydrothermal flow treatment on the structure and morphology of synthesised materials. The

MAX precursor prior to being treated in CHFS was subjected to HF treatment (to remove Al layers) followed by ultrasonication in DMSO. SEM images shown in Fig.3 reveal the characteristic MXene phase  $Ti_2C$ . Furthermore, as shown in the SEM images (**Fig. 4**), as-prepared N-MXene/ $TiO_2$  (NMT) composites exhibit accordion-like and separated sheet structures with spherical nanoparticles distributed across the surface of the sheets. These nanoparticles were formed in both NMT350 and NMT450 samples due to the supercritical environment created during hydrothermal treatment at  $350^\circ C$  and  $450^\circ C$ , which can be related to the controlled oxidation of MXene to  $TiO_2$ .

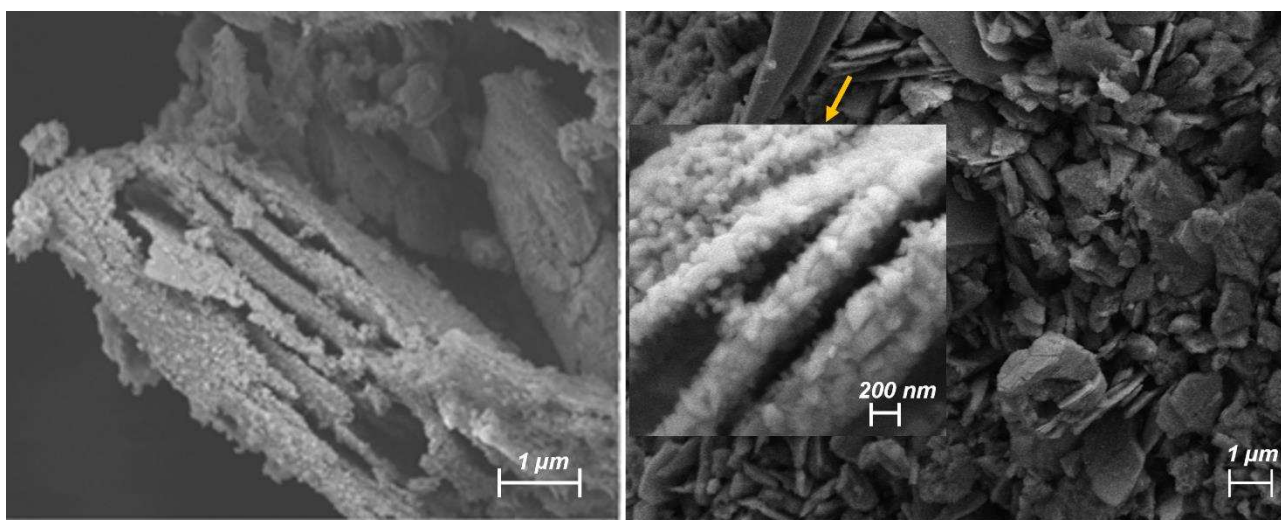


**Fig. 4** SEM images of N-MXene/ $TiO_2$  nanocomposites produced via continuous hydrothermal flow synthesis showing a sandwich arrangement with  $TiO_2$  nanoparticles embedded in between MXene sheets.

The surface of the MXene sheets appears “rough” after hydrothermal treatment due to the formation of titania nanoparticles on its surface compared to pre-treated delaminated MXene (**Fig. 3**). EDS analysis (Fig.S1 and Table S1) confirmed the presence of  $TiO_2$  particles.

It is hypothesised that the oxidation of MXene sheets starts from the edges due to the presence of these spherical nanoparticles observed around the edges (inset **Fig. 4**), which later extends to the core as reaction temperature increases to  $450^\circ C$ . The structure of the N-doped MXene/ $TiO_2$  (NMT) composites shows a sandwich arrangement with  $TiO_2$

nanoparticles embedded in between MXene sheets. It is envisaged that this arrangement helps keep MXene sheets separated, thereby making them accessible for intercalation of  $\text{Li}^+$  ions and promoting its surface area access to electrolyte ions. EDS analysis (Fig.S1 and Table S1) confirmed the presence of  $\text{TiO}_2$  particles.

The high-resolution transmission electron microscopy (HRTEM) images and measurements of lattice fringes show a distribution of nanoparticles on the MXene sheets in a sandwich arrangement (**Fig. 5**). HRTEM images further show that  $\text{Ti}_2\text{CT}_x$  exists in single and few-layered nanosheets with nanoparticles grown on the surface of MXene (**Fig. 5g**).

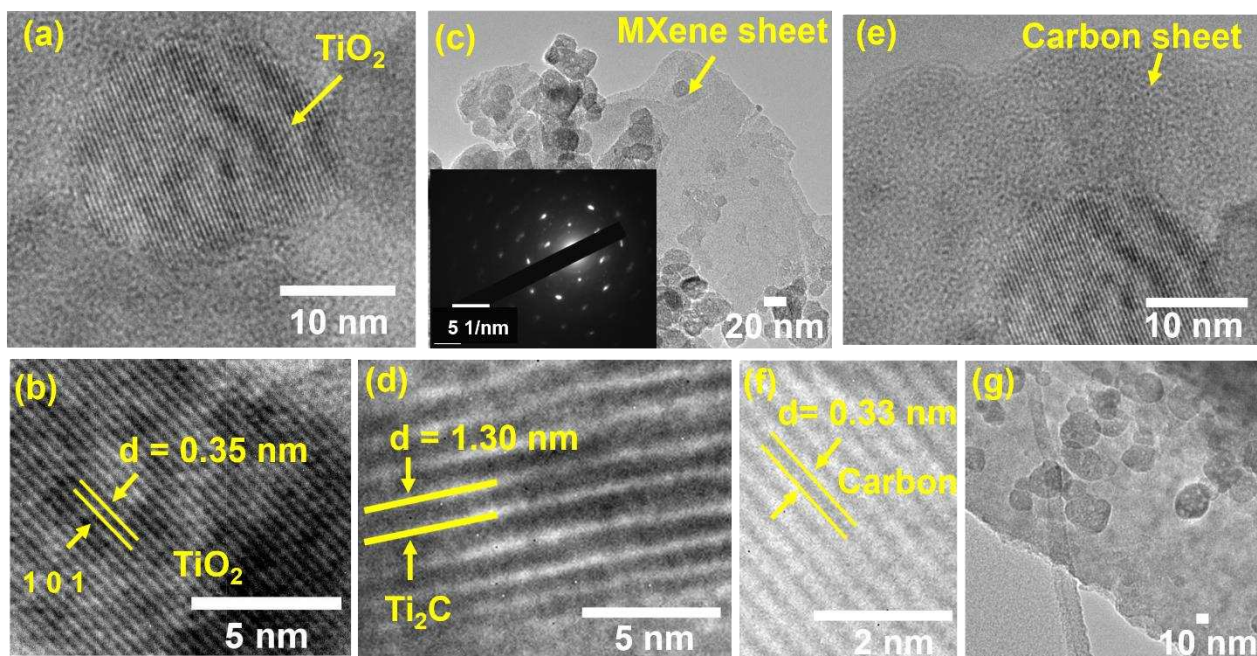


**Fig. 5** High-resolution transmission electron microscopy images with selected area electron diffraction (inset) of MXene hybrids consisting of anatase  $\text{TiO}_2$  (lattice fringe spacing of  $d = 0.35$  nm),  $\text{Ti}_2\text{C}$  MXene ( $d = 1.30$  nm), and carbon ( $d = 0.33$  nm).

HRTEM also reveals the lattice planes of anatase  $\text{TiO}_2$ ,  $\text{Ti}_2\text{C}$  MXene, and carbonaceous carbon (**Fig. 5b, 5d & 5f**) with parallel fringe spacings of 0.35 nm and 1.30 nm for  $\text{TiO}_2$  and  $\text{Ti}_2\text{C}$  MXene, respectively. A  $d$ -spacing of 0.33 nm is also measured in the HRTEM image, which can be attributed to graphitic carbon[41]. The selected area electron diffraction

(SAED) pattern shows that MXene retained the hexagonal symmetry (inset image in **Fig. 5c**)[2,32,42,43].

XPS analysis was carried out to determine the elemental composition and surface chemistry of the NMT nanocomposites. The acquired survey spectrum (**Fig. 6a**) for each sample shows the presence of titanium (Ti), carbon (C), nitrogen (N), oxygen (O), and fluorine (F).

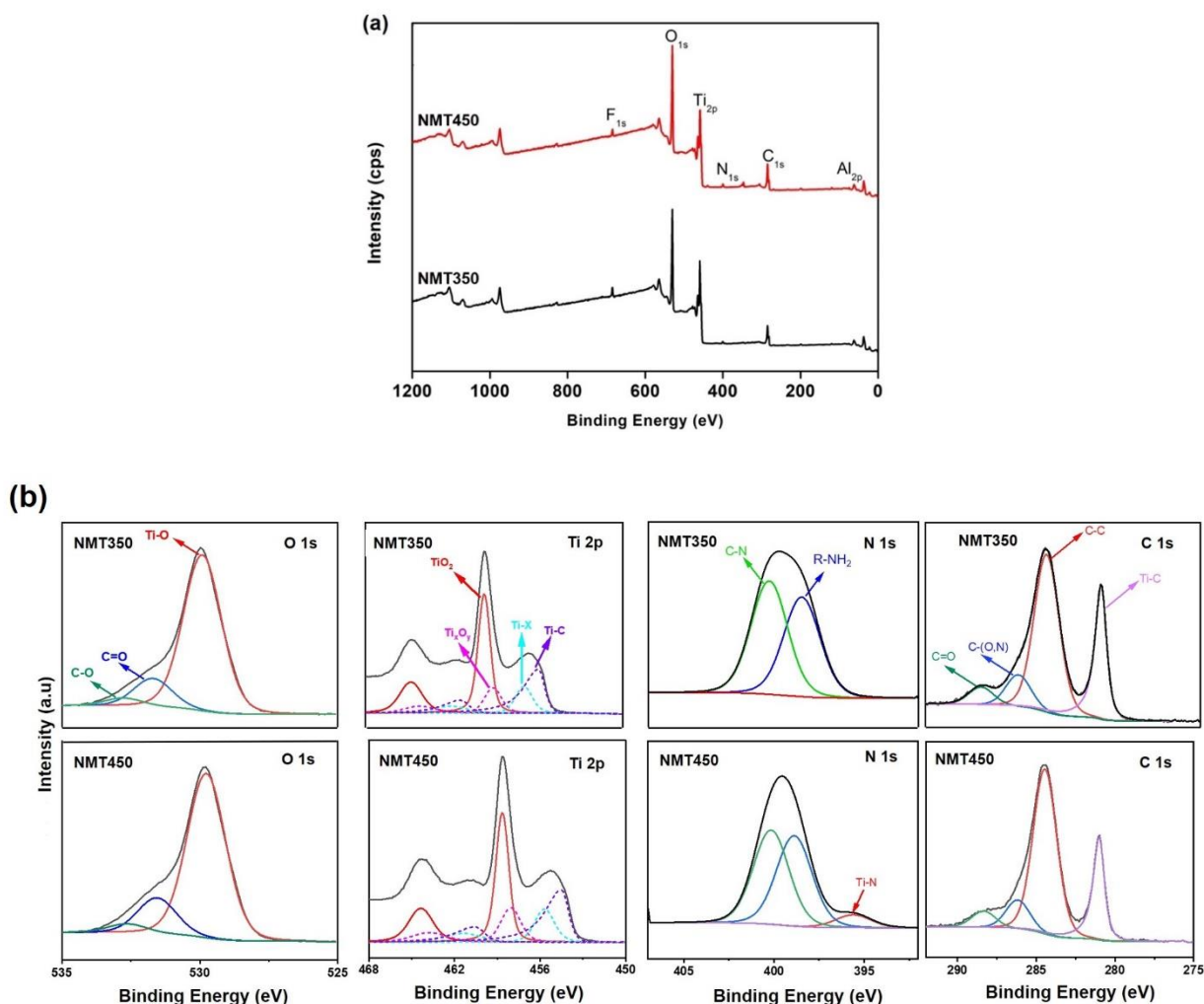


**Fig. 6 (a)** XPS survey scans **(b)** High-resolution spectra of C(1s), N(1s), O(1s) and Ti(2p) core levels showing the chemical bonding states in NMT nanocomposites. Three distinct doping sites in N-MXene were observed attributable to surface absorption (400.8 eV), surface functional site substitution (399.1 eV), or lattice substitution (395.6 eV).

The high-resolution Ti 2p spectrum of NMT samples was fitted with four doublet pairs (Ti 2p<sub>3/2</sub> and Ti 2p<sub>1/2</sub>) with a fixed area ratio equal to 2:1 and a doublet separation of 5.7 eV, note for clarity, the fits of the Ti 2p spectra are shown offset from the photoelectron speaks after subtraction of a Shirley background. The Ti 2p<sub>3/2</sub> components are positioned at 458.9 eV, 458.0 eV, 455.7 eV and 454.6 eV. The Ti 2p<sub>3/2</sub> component centred at 458.9 eV is dominant associated with Ti<sup>4+</sup> ions, indicating the presence of TiO<sub>2</sub>, and the lower binding Ti 2p<sub>3/2</sub> component at 458.0 eV is associated with reduced charge state titanium ions (Ti<sub>x</sub>O<sub>y</sub>). The Ti 2p<sub>3/2</sub> component centred at 455.7 eV represents sub-stoichiometric titanium oxide or oxycarbides, and the Ti 2p<sub>3/2</sub> component centred at 454.6 eV is assigned to Ti-C bonds present in the composites[44–46]. Ti<sub>2</sub>C was not completely converted to TiO<sub>2</sub>; this can be seen in the XPS spectrum of C1s core level showing the presence of Ti-C bonds due to component located at 281.1 eV along with other components at 288.6 eV, and 284.7 eV corresponding to (O-C=O and C-F), C-O and C-C (sp<sub>2</sub>) bonds respectively[40,44]. The presence of the N 1s signal further confirms the exciting chemistry of functionalising MXene using CHFS via doping with nitrogen atoms to enhance its electronic properties. The high-resolution N 1s spectrum could be fitted with two peaks centred at 400.8 eV and 399.1 eV corresponding to protonated pyridinic nitrogen and pyrrolic nitrogen respectively[32,47]. An absence of Ti-N peak (395.6 eV) at 350 °C indicates that the substitution of carbon atom in the Ti<sub>2</sub>C lattice structure with nitrogen atoms did not begin until about a temperature of 400°C (**Fig. 6a & 6b**). In addition, from elemental analysis an increase in nitrogen uptake (from 1.60 % to 2.14 %) with a corresponding decrease in the F-surface terminations (from 2.90 % to 1.94 %) is observed as the reaction temperature increased from 350 °C to 450 °C. This observation agrees with previously reported data on N-doped MXenes from literature<sup>17</sup>.

To determine the crystalline phase structures, present in the NMT nanocomposites and the effect of hydrothermal treatment on the d-spacing of Ti<sub>2</sub>C, XRD analysis (**Fig. 7a**) was

carried out. Relatively sharp diffraction peaks of crystalline  $\text{TiO}_2$  were observed at  $2\theta = 25.3^\circ, 37.2^\circ, 47.8^\circ$  and  $54.1^\circ$ , which corresponds to the (101), (004), (200), and (105) peaks of anatase  $\text{TiO}_2$  (JCPDS card no. 21-1271)[40,44,48]. The intensity of these peaks (especially 101 peaks) can be observed to increase as temperature increases from  $350^\circ\text{C}$  to  $450^\circ\text{C}$ , indicating more  $\text{TiO}_2$  being formed. However, the (002) peak of  $\text{Ti}_2\text{C}$  MXene shifts to a lower angle of  $2\theta = 7^\circ$  as compared to the starting material (*d*-MXene), indicating an increase in interlayer distance resulting from  $\text{TiO}_2$  formation in between MXene sheets after heating[42]. A peak at  $14.5^\circ$  is also observed and can be attributed to carbon. The presence of titania, MXene and carbon diffraction patterns are consistent with the observations from HRTEM analyses. According to the Scherrer equation, the average size of  $\text{TiO}_2$  nanoparticles in NMT350 and NMT450 is 32 nm and 34 nm, respectively. The XRD pattern also shows that the (002) diffraction peaks of  $\text{Ti}_2\text{AlC}$  broadened with a shift towards lower angles, indicating an increase in *d*-spacing in the MXene sample due to removal of Al layer. In addition, (002) peak is the dominant peak, indicating the majority of the NMT nanocomposite is the MXene phase. Based on the Rietveld refinement, we observed a 12% and 27% composition of  $\text{TiO}_2$  in NMT350 and NMT450 respectively, which is a two-fold increase in  $\text{TiO}_2$  from  $350^\circ\text{C}$  to  $450^\circ\text{C}$ . However, this increment is not greatly reflected in an increase in the specific capacity of the NMT composites, as  $\text{TiO}_2$  contributes primarily as a spacer between MXene sheets to prevent re-stacking.

To observe the change in the electronic properties and vibrational modes of untreated  $\text{Ti}_2\text{C}$  and NMT nanocomposites, the Raman technique was used. The Raman spectra below (**Fig. 7b**) show the constituents of the prepared samples. A prominent Raman peak centred at  $149\text{ cm}^{-1}$  corresponds to anatase  $\text{TiO}_2$ , whose intensity increases as temperature increases, signifying more  $\text{TiO}_2$  formation[43,48]. Also shown are three Raman peaks centred at  $250\text{ cm}^{-1}$ ,  $410\text{ cm}^{-1}$ , and  $612\text{ cm}^{-1}$  attributed to vibrations from  $\text{Ti}_2\text{C}$ [50]. These peaks are

observed to exhibit a redshift as temperature increases owing to thinning of MXene layers. D and G peaks at  $1347\text{ cm}^{-1}$  and  $1588\text{ cm}^{-1}$ , respectively, indicate the formation of graphitic carbon during the hydrothermal process, which increases with temperature[40]. The G band is attributed to the  $E_{2g}$  vibration modes of  $sp^2$  carbon atoms associated with the graphitic core, while the D band represents the  $sp^3$  carbon atoms.

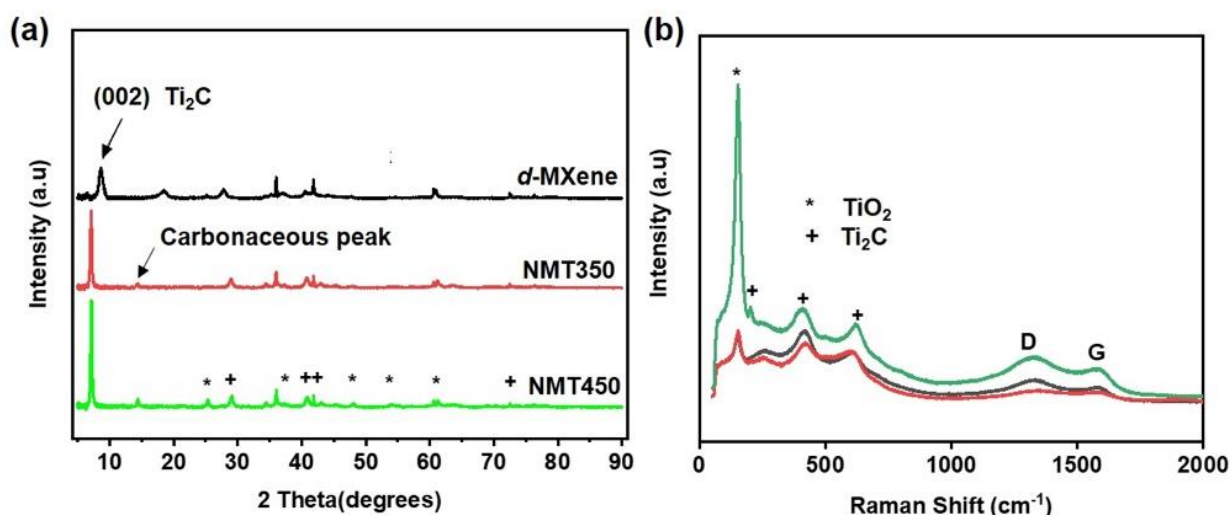


**Fig. 7(a)** XRD patterns and **(b)** Raman spectra of NMT nanocomposites showing the presence of  $Ti_2C$ , anatase titania and formation of carbon.

The composites were prepared into electrodes as a binder-free Li-ion anode material via aqueous processing. Viscous slurries of the NMT material synthesised using both the upper and lower processing temperatures in the CHFS reactor (i.e.  $450\text{ }^{\circ}\text{C}$  or  $350\text{ }^{\circ}\text{C}$ ) were prepared by dispersing the material in de-ionised water in a ratio of 1:10 w/v and then stirring for 12 hours. The slurries were subsequently coated onto a Cu foil substrate and dried. Notably, no polymeric binders or conductive anodes were required to fabricate the electrodes, unlike conventional anode materials for LIBs. The electrochemical performance of the NMT electrodes was evaluated by cyclic voltammetry and galvanostatic cycling in the voltage range of 0 – 3 V versus Li/Li<sup>+</sup> in a 1 M LiPF<sub>6</sub> in EC/DMC (1:1 v/v) electrolyte (**Fig. 8**). **Fig. 8a** shows the cyclic voltammogram of the NMT350 electrode using a sweep rate of

0.1 mV s<sup>-1</sup>. The same analysis was performed on the NMT450 electrode and is presented in **Fig. 8b**. A distinct lithiation peak occurs at 0.6 V in the first cycle, which disappears subsequently and is related to the formation of the solid electrolyte interphase (SEI) layer. The shape of the CV curves match previously reported MXene derived materials, with broad peaks in the range of 1.0 V to 2.0 V occurring during both lithiation and de-lithiation associated with the reversible intercalation of Li<sup>+</sup> in Ti<sub>2</sub>C. Evidence of the reversible insertion of lithium in TiO<sub>2</sub> is also present from the CV curves, with a coincident peak occurring at 2.0 V attributed to the oxidation of the TiO<sub>2</sub>[51,52].

The cycle stability of the NMT material was assessed via galvanostatic cycling using a current density of 30 mA g<sup>-1</sup>, with results shown in **Fig. 8c**. Both NMT350 and NMT450 electrodes offer excellent capacity retention over extended cycles. The stability of the material is notable, considering that no binders or conductive additives were used to prepare the electrodes. In both cases, the material undergoes an activation process. The gravimetric capacity of NMT350 increases from an initial value of 305 mAh g<sup>-1</sup> at cycle 3 to 369 mAh g<sup>-1</sup> after 100 cycles, while NMT450 shows an initial gravimetric capacity of 313 mAh g<sup>-1</sup> increasing to 355 mAh g<sup>-1</sup> over its cycling range. This behaviour has previously been reported for TiO<sub>2</sub>-based anodes and is similar to activation phenomena for other transition metal-based oxide electrode materials[53–55]. Furthermore, the increasing capacity can be attributed to the fact that repeated intercalation and de-intercalation of Li<sup>+</sup> in Ti<sub>2</sub>C causes a gradual increase in the interlayer space, enhancing the lithiation capacity of the material[56–58]. Post-mortem SEM analysis of the NMT anodes after extended cycling indicate that the individual MXene sheets have further separated and are reduced in size compared to the material prior to cycling (**Supporting Info Fig. S2**).

The coulombic efficiency of the NMT350 and NMT450 electrodes increases from an initial value of 40.2% and 19.4% to an average of 99.7% and 99.1% respectively for the last five

cycles (**Supporting Info Fig. S3**). To benchmark the performance of the NMT electrodes, it was compared to the galvanostatic cycling behaviour of the untreated MXene precursor material (**Supporting Info Fig. S4**). Notably, the performance of the NMT electrodes was far superior to the control, which exhibited a lower initial capacity of 252 mAh g<sup>-1</sup> that gradually decreased over the next 20 cycles before plateauing at 140 mAh g<sup>-1</sup>. The enhancement in the gravimetric capacity of the NMT electrodes is due to the sandwich arrangement of the material, with TiO<sub>2</sub> nanoparticles increasing the accessibility of the Li<sup>+</sup> ions through separation of the Ti<sub>2</sub>C sheets (**Fig. 4**). TiO<sub>2</sub> plays a dual role as it also electrochemically active and contributes to the capacity through the reversible insertion and removal of Li<sup>+</sup> ions during charging and discharging.

The electrochemical processes occurring during cycling were further assessed through analysis of the voltage profiles and differential capacity plots of the electrodes. **Fig. 8d and 8e** shows the voltage profile and differential capacity plot of the 10<sup>th</sup> cycle of the NMT350 electrode. The sloping shape of the voltage profiles shows that lithium is stored over a wide potential range (**Fig 8d**). The differential capacity plot shows (**Fig. 8e**) that a dominant and broad peak occurs between 1.0 V and 2.0 V during charging and discharging. This potential region is associated with both the intercalation of Li<sup>+</sup> in Ti<sub>2</sub>C and lithium insertion into anatase TiO<sub>2</sub>. In the differential capacity plot for the untreated MXene (**Fig. 8e**), the peak between 1.0 V and 2.0 V is far less prominent, indicating the prohibition of the interlayer accessibility of Li<sup>+</sup> ions due to the absence of the enhanced separation that TiO<sub>2</sub> provides in the NMT material. Notably, as described in the literature, an increase in the surface area of MXenes either by oxidation or delamination creates a considerable increase in its specific capacity [41,44]. This observation illustrates the benefit of processing the material in the CHFS reactor as both the specific capacity and capacity retention increase compared to untreated delaminated MXene due to the enhancing properties of TiO<sub>2</sub>.

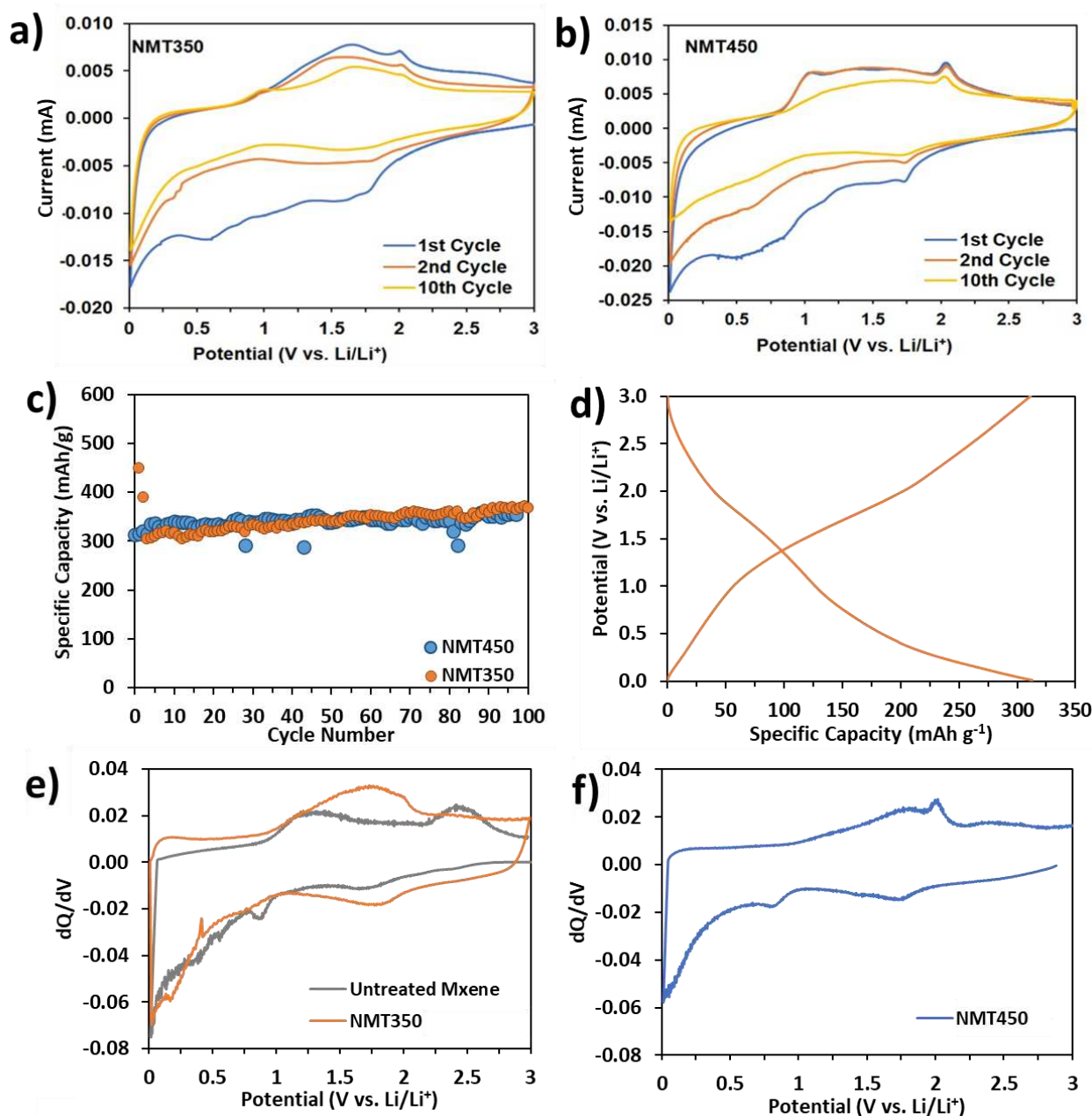


**Fig. 8** (a) Cyclic voltammogram of the 1<sup>st</sup>, 2<sup>nd</sup> and 10<sup>th</sup> cycle of NMT350 half-cell using a sweep rate of 0.1 mV/s in the potential range of 0 – 3 V. (b) Cyclic voltammogram of the 1<sup>st</sup>, 2<sup>nd</sup> and 10<sup>th</sup> cycle of NMT450 half-cell using a sweep rate of 0.1 mV/s in the potential range of 0 – 3 V. (c) Specific discharge capacities of the NMT350 and NMT450 electrodes using a current density of 30 mA/g in the potential region of 0 – 3 V. (d) Voltage profile of the 10<sup>th</sup> cycle of the NMT350 electrode cycled in c). (e) Differential capacity plots of the 10<sup>th</sup> cycle of the NMT350 electrode overlaid with that of the untreated MXene electrode. (f) Differential capacity plot of the 10<sup>th</sup> cycle of the NMT450 electrode.

The voltage profiles (**Supporting Info Fig. S5**) and differential capacity plots (**Fig. 8f**) of the NMT450 electrode have very similar shapes to the NMT350 electrode. However, a more pronounced peak at 2.0 V in the differential capacity plot is observed that can be attributed to the increased concentration of TiO<sub>2</sub> in the NMT450 nanomaterial synthesised at a higher temperature. Rate capability testing of the MXene electrodes produced initial specific discharge capacities of 177 mAh/g (untreated MXene), 288 mAh/g (NMT350) and 310 mAh/g (NMT450) at a C/10 rate (**Supporting Info Fig. S6**). Furthermore, the NMT350 and NMT450 exhibited higher capacities than the untreated MXene control electrode at rates of C/5, C/2 and 1C, however at the faster rates of 2C, 5C and 10C, the control electrode behaved similarly to the N-MXene/TiO<sub>2</sub> composites in terms of exhibited capacity.

#### 4. Conclusions

Herein, a controlled single-step hydrothermal synthesis of NMT nanocomposites was developed using Ti<sub>2</sub>C MXene and ammonia as water-soluble precursors. The CHFS methodology shows an economically feasible means of nitrogen-doping and controlled in-situ synthesis of TiO<sub>2</sub> nanoparticles from MXenes. The as-synthesised NMT nanomaterials were fabricated into electrodes without the use of binders as a Li-ion anode material. The NMT nanocomposite electrodes underwent an activation process and obtained a specific capacity of 305 mAh g<sup>-1</sup> initially, increasing to 369 mAh g<sup>-1</sup> after 100 cycles. NMT also exhibit stable capacity retention and are more environmentally friendly than conventional materials such as graphite. The electrochemical performance of NMT nanocomposites synthesised via CHFS in a fraction of a second exceeds that of N-doped MXenes prepared via annealing at 700 °C for 2h[17]. Furthermore, the as-synthesised NMT nanocomposites outperform reported Ti<sub>2</sub>C-carbon nanocomposites in specific capacity and rate capability. CHFS synthesised materials performed well electrochemically, however because NMT350 is synthesised at a lower temperature, we conclude it is the optimum material. To conclude, CHFS offers an environmentally friendly synthetic approach for engineering NMT

nanocomposites as promising Li-ion anode materials. Furthermore, the electrodes are fabricated via aqueous processing, thereby eliminating the need for harsh solvents. On the whole, this work adds to the expanding portfolio of CHFS materials in the development of rapid and clean hydrothermal technologies for energy storage applications.

## Acknowledgements

The authors would like to acknowledge LSBU for all the support provided in the completion of this research work and EPSRC Grand Challenge fund (DAN, SF090420SK/ T090420SK). Kieran McCarthy would like to acknowledge financial support from the Irish Research Council (IRC) and Analog Devices International (ADI), under the IRC Enterprise Award Scheme (contract no. EPSPG/2017/377). Further acknowledgements are extended to the Open University Electron Microscopy Suite, Dr. Zeeshan Mughal, Dr. Radka Gromnicova, and Dr. Igor Kraev, for their support on electron microscopy of all samples. XPS data collection was performed at the EPSRC National Facility for XPS ('HarwellXPS'), operated by Cardiff University and UCL, under contract No. PR16195. Ioan-Alexandru Baragau would like to acknowledge funding through the Romanian Ministry of Research and Innovation (Core Program 21N-PN19-030101).

## References

- [1] S. Kajiyama, L. Szabova, K. Sodeyama, H. Iinuma, R. Morita, K. Gotoh, Y. Tateyama, M. Okubo, A. Yamada, Sodium-Ion Intercalation Mechanism in MXene Nanosheets, *ACS Nano*. 10 (2016) 3334–3341. <https://doi.org/10.1021/acsnano.5b06958>.
- [2] D. Xiong, X. Li, Z. Bai, S. Lu, Recent Advances in Layered  $Ti_3C_2T_x$  MXene for Electrochemical Energy Storage, *Small*. 14 (2018) 1703419. <https://doi.org/10.1002/smll.201703419>.
- [3] C. Daniel, D. Mohanty, J. Li, D.L. Wood, Cathode Materials Review, *AIP Conf. Proc.* 1597 (2014) 26–43. <https://doi.org/10.1063/1.4878478>.
- [4] N.M. Morris, Storage Devices and Systems, in: *Digit. Tech.*, 1979: pp. 94–104. [https://doi.org/10.1007/978-1-349-04624-9\\_11](https://doi.org/10.1007/978-1-349-04624-9_11).
- [5] C. (John) Zhang, V. Nicolosi, Graphene and MXene-Based Transparent Conductive Electrodes and

- Supercapacitors, *Energy Storage Mater.* 16 (2019) 102–125.  
<https://doi.org/10.1016/j.ensm.2018.05.003>.
- [6] S.J. Kim, M. Naguib, M. Zhao, C. Zhang, H.T. Jung, M.W. Barsoum, Y. Gogotsi, High Mass Loading, Binder-Free MXene Anodes for High Areal Capacity Li-ion batteries, *Electrochim. Acta.* 163 (2015) 246–251. <https://doi.org/10.1016/j.electacta.2015.02.132>.
- [7] P. Yu, G. Cao, S. Yi, X. Zhang, C. Li, X. Sun, K. Wang, Y. Ma, Binder-Free 2D Titanium Carbide (MXene)/Carbon Nanotube Composites for High-Performance Lithium-Ion Capacitors, *Nanoscale.* 10 (2018) 5906–5913. <https://doi.org/10.1039/c8nr00380g>.
- [8] H. Darjazi, A. Staffolani, L. Sbrascini, L. Bottoni, R. Tossici, F. Nobili, Sustainable Anodes for Lithium- and Sodium-Ion Batteries Based on Coffee Ground-Derived Hard Carbon and Green Binders, *Energies.* 13 (2020) 6216. <https://doi.org/10.3390/en13236216>.
- [9] S.F. Lux, F. Schappacher, A. Balducci, S. Passerini, M. Winter, Low Cost, Environmentally Benign Binders for Lithium-Ion Batteries, *J. Electrochem. Soc.* 157 (2010) A320.  
<https://doi.org/10.1149/1.3291976>.
- [10] L. Zhang, L. Chai, Q. Qu, L. Zhang, M. Shen, H. Zheng, Chitosan, a New and Environmental Benign Electrode Binder for Use with Graphite Anode in Lithium-Ion Batteries, *Electrochim. Acta.* 105 (2013) 378–383. <https://doi.org/10.1016/j.electacta.2013.05.009>.
- [11] J. Chong, S. Xun, H. Zheng, X. Song, G. Liu, P. Ridgway, J.Q. Wang, V.S. Battaglia, A Comparative Study of Polyacrylic Acid and Poly(vinylidene difluoride) Binders for Spherical Natural Graphite/LiFePO<sub>4</sub> Electrodes and Cells, *J. Power Sources.* 196 (2011) 7707–7714.  
<https://doi.org/10.1016/j.jpowsour.2011.04.043>.
- [12] S. Lim, H. Park, J. Yang, C. Kwak, J. Lee, Stable colloidal dispersion of octylated Ti<sub>3</sub>C<sub>2</sub>-MXenes in a Nonpolar Solvent, *Colloids Surfaces A Physicochem. Eng. Asp.* 579 (2019) 123648.  
<https://doi.org/10.1016/j.colsurfa.2019.123648>.
- [13] B. Anasori, M.R. Lukatskaya, Y. Gogotsi, 2D Metal Carbides and Nitrides (MXenes) for Energy Storage, *Nat. Rev. Mater.* 2 (2017) 16098. <https://doi.org/10.1038/natrevmats.2016.98>.
- [14] U. Alli, S.J. Hettiarachchi, S. Kellici, Chemical Functionalisation of 2D Materials by Batch and Continuous Hydrothermal Flow Synthesis, *Chem. - A Eur. J.* (2020) 6447–6460.  
<https://doi.org/10.1002/chem.202000383>.
- [15] M. Naguib, M. Kurtoglu, V. Presser, J. Lu, J. Niu, M. Heon, L. Hultman, Y. Gogotsi, M.W. Barsoum, Two-Dimensional Nanocrystals Produced by Exfoliation of Ti<sub>3</sub>AlC<sub>2</sub>, *Adv. Mater.* 23 (2011) 4248–4253.  
<https://doi.org/10.1002/adma.201102306>.

- [16] Z. Fan, Y. Wang, Z. Xie, D. Wang, Y. Yuan, H. Kang, B. Su, Z. Cheng, Y. Liu, Modified MXene/Holey Graphene Films for Advanced Supercapacitor Electrodes with Superior Energy Storage, *Adv. Sci.* 5 (2018) 18000750. <https://doi.org/10.1002/advs.201800750>.
- [17] Y. Wen, T.E. Rufford, X. Chen, N. Li, M. Lyu, L. Dai, L. Wang, Nitrogen-Doped  $\text{Ti}_3\text{C}_2\text{T}_x$  MXene Electrodes for High-Performance Supercapacitors, *Nano Energy*. 38 (2017) 368–376. <https://doi.org/10.1016/j.nanoen.2017.06.009>.
- [18] S.S. El-Deen, A.M. Hashem, A.E. Abdel Ghany, S. Indris, H. Ehrenberg, A. Mauger, C.M. Julien, Anatase  $\text{TiO}_2$  Nanoparticles for Lithium-Ion Batteries, *Ionics (Kiel)*. 24 (2018) 2925–2934. <https://doi.org/10.1007/s11581-017-2425-y>.
- [19] T. Song, U. Paik,  $\text{TiO}_2$  as an Active or Supplemental Material for Lithium Batteries, *J. Mater. Chem. A*. 4 (2015) 14–31. <https://doi.org/10.1039/c5ta06888f>.
- [20] B. Qiu, M. Xing, J. Zhang, Mesoporous  $\text{TiO}_2$  Nanocrystals Grown In-situ on Graphene Aerogels for High Photocatalysis and Lithium-Ion Batteries, *J. Am. Chem. Soc.* 136 (2014) 5852–5855. <https://doi.org/10.1021/ja500873u>.
- [21] B.A. Bhanvase, T.P. Shende, S.H. Sonawane, A Review on Graphene– $\text{TiO}_2$  and Doped Graphene– $\text{TiO}_2$  Nanocomposite Photocatalyst for Water and Wastewater Treatment, *Environ. Technol. Rev.* 6 (2017) 1–14. <https://doi.org/10.1080/21622515.2016.1264489>.
- [22] K. Hashimoto, H. Irie, A. Fujishima,  $\text{TiO}_2$  Photocatalysis: A Historical Overview and Future Prospects, *Assoc. Asia Pacific Phys. Soc. Bull.* 44 (2007) 8269.
- [23] S.Y. Lee, S.J. Park,  $\text{TiO}_2$  photocatalyst for Water Treatment Applications, *J. Ind. Eng. Chem.* 19 (2013) 1761–1769. <https://doi.org/10.1016/j.jiec.2013.07.012>.
- [24] Y. Liu, Y. Yang, Recent progress of  $\text{TiO}$ -Based Anodes for Li-Ion Batteries, *J. Nanomater.* 2016 (2016). <https://doi.org/10.1155/2016/8123652>.
- [25] X. Du, Q. Wang, T. Feng, X. Chen, L. Li, L. Li, X. Meng, L. Xiong, X. Sun, L. Lu, Y. Xu, One-Step Preparation of Nanoarchitected  $\text{TiO}_2$  on Porous Al as Integrated Anode for High-performance Lithium-ion Batteries, *Sci. Rep.* 6 (2016) 20138. <https://doi.org/10.1038/srep20138>.
- [26] Y. Li, C. Ou, Y. Huang, Y. Shen, N. Li, H. Zhang, Towards Fast and Ultralong-Life Li-ion battery Anodes: Embedding Ultradispersed  $\text{TiO}_2$  Quantum Dots into Three-Dimensional Porous Graphene-like Networks, *Electrochim. Acta.* 246 (2017) 1183–1192. <https://doi.org/10.1016/j.electacta.2017.06.152>.
- [27] W. Wang, Y. Liu, X. Wu, J. Wang, L. Fu, Y. Zhu, Y. Wu, X. Liu, Advances of  $\text{TiO}_2$  as Negative Electrode Materials for Sodium-Ion Batteries, *Adv. Mater. Technol.* 3 (2018) 1800004.

<https://doi.org/10.1002/ADMT.201800004>.

- [28] S. Moitzheim, S. De Gendt, P.M. Vereecken, Investigation of the Li-Ion Insertion Mechanism for Amorphous and Anatase TiO<sub>2</sub> Thin-Films, *J. Electrochem. Soc.* 166 (2019) A1–A9.  
<https://doi.org/10.1149/2.1091816jes>.
- [29] Y. Li, C. Ou, Y. Huang, Y. Shen, N. Li, H. Zhang, Towards Fast and Ultralong-Life Li-ion Battery Anodes: Embedding Ultradispersed TiO<sub>2</sub> Quantum Dots into Three-Dimensional Porous Graphene-like Networks, *Electrochim. Acta.* 246 (2017) 1183–1192.  
<https://doi.org/10.1016/j.electacta.2017.06.152>.
- [30] P.W. Dunne, A.S. Munn, C.L. Starkey, E.H. Lester, The Sequential Continuous Flow Hydrothermal Synthesis of Molybdenum Disulphide, *Chem. Commun.* 51 (2015) 4048–4050.  
<https://doi.org/10.1039/c4cc10158h>.
- [31] E. Lester, P. Blood, J. Denyer, D. Giddings, B. Azzopardi, M. Poliakoff, Reaction Engineering: The Supercritical Water Hydrothermal Synthesis of Nanoparticles, *J. Supercrit. Fluids.* 37 (2006) 209–214.  
<https://doi.org/10.1016/j.supflu.2005.08.011>.
- [32] I.A. Baragau, N.P. Power, D.J. Morgan, T. Heil, R.A. Lobo, C.S. Roberts, M.M. Titirici, S. Dunn, S. Kellici, Continuous Hydrothermal Flow Synthesis of Blue-Luminescent, Excitation-Independent Nitrogen-Doped Carbon Quantum Dots as Nanosensors, *J. Mater. Chem. A.* 8 (2020) 3270–3279.  
<https://doi.org/10.1039/c9ta11781d>.
- [33] A.J. Hunt, T.M. Attard, *Supercritical and Other High-pressure Solvent Systems*, Royal Society of Chemistry, Cambridge, 2018. <https://doi.org/10.1039/9781788013543>.
- [34] S. Kellici, J. Acord, N.P. Power, D.J. Morgan, P. Coppo, T. Heil, B. Saha, Rapid synthesis of Graphene Quantum Dots Using a Continuous Hydrothermal Flow Synthesis Approach, *RSC Adv.* 7 (2017) 14716–14720. <https://doi.org/10.1039/c7ra00127d>.
- [35] J.A. Darr, J. Zhang, N.M. Makwana, X. Weng, Continuous Hydrothermal Synthesis of Inorganic Nanoparticles: Applications and Future Directions, *Chem. Rev.* 117 (2017) 11125–11238.  
<https://doi.org/10.1021/acs.chemrev.6b00417>.
- [36] S. Kellici, J. Acord, A. Vaughn, N.P. Power, D.J. Morgan, T. Heil, S.P. Facq, G.I. Lampronti, Calixarene Assisted Rapid Synthesis of Silver-Graphene Nanocomposites with Enhanced Antibacterial Activity, *ACS Appl. Mater. Interfaces.* 8 (2016) 19038–19046.  
<https://doi.org/10.1021/acsami.6b06052>.
- [37] A. Vaughn, J. Ball, T. Heil, D.J. Morgan, G.I. Lampronti, G. Maršalkaitė, C.L. Raston, N.P. Power, S. Kellici, Selective Calixarene-Directed Synthesis of MXene Plates, Crumpled Sheets, Spheres, and

- Scrolls, Chem. - A Eur. J. 23 (2017) 8128–8133. <https://doi.org/10.1002/chem.201701702>.
- [38] S. Kellici, J. Acord, J. Ball, H.S. Reehal, D. Morgan, B. Saha, A Single Rapid Route for the Synthesis of Reduced Graphene Oxide with Antibacterial Activities, RSC Adv. 4 (2014) 14858–14861. <https://doi.org/10.1039/c3ra47573e>.
- [39] Z. Zhang, S. Brown, J.B.M. Goodall, X. Weng, K. Thompson, K. Gong, S. Kellici, R.J.H. Clark, J.R.G. Evans, J.A. Darr, Direct Continuous Hydrothermal Synthesis of High Surface Area Nanosized Titania, J. Alloys Compd. 476 (2009) 451–456. <https://doi.org/10.1016/j.jallcom.2008.09.036>.
- [40] X. Zhang, Y. Liu, S. Dong, Z. Ye, Y. Guo, One-Step Hydrothermal Synthesis of a TiO<sub>2</sub>-Ti<sub>3</sub>C<sub>2</sub>T<sub>x</sub> Nanocomposite with Small Sized TiO<sub>2</sub> Nanoparticles, Ceram. Int. 43 (2017) 11065–11070. <https://doi.org/10.1016/j.ceramint.2017.05.151>.
- [41] M. Naguib, O. Mashtalir, ... M.L.-C., U. 2014, One-Step Synthesis of Nanocrystalline Transition Metal Oxides on Thin Sheets of Disordered Graphitic Carbon by Oxidation of MXenes, Pubs.Rsc.Org. 50 (2014) 7420–7423. <https://pubs.rsc.org/en/content/articlehtml/2014/cc/c4cc01646g> (accessed June 1, 2021).
- [42] J. Li, Y. Du, C. Huo, S. Wang, C. Cui, Thermal Stability of Two-Dimensional Ti<sub>2</sub>C Nanosheets, Ceram. Int. 41 (2015) 2631–2635. <https://doi.org/10.1016/j.ceramint.2014.10.070>.
- [43] X. Li, X. Yin, M. Han, C. Song, X. Sun, H. Xu, L. Cheng, L. Zhang, A Controllable Heterogeneous Structure and Electromagnetic Wave Absorption Properties of Ti<sub>2</sub>CT<sub>x</sub>: X MXene, J. Mater. Chem. C. 5 (2017) 7621–7628. <https://doi.org/10.1039/c7tc01991b>.
- [44] B. Ahmed, D.H. Anjum, M.N. Hedhili, Y. Gogotsi, H.N. Alshareef, H<sub>2</sub>O<sub>2</sub> Assisted Room Temperature Oxidation of Ti<sub>2</sub>C MXene for Li-ion battery anodes, Nanoscale. 8 (2016) 7580–7587. <https://doi.org/10.1039/c6nr00002a>.
- [45] B. Mendoza-Sánchez, Y. Gogotsi, Synthesis of Two-Dimensional Materials for Capacitive Energy Storage, Adv. Mater. 28 (2016) 6104–6135. <https://doi.org/10.1002/adma.201506133>.
- [46] K. Zhu, Y. Jin, F. Du, S. Gao, Z. Gao, X. Meng, G. Chen, Y. Wei, Y. Gao, Synthesis of Ti<sub>2</sub>CT<sub>x</sub> MXene as Electrode Materials for Symmetric Supercapacitor with Capable Volumetric Capacitance, J. Energy Chem. 31 (2019) 11–18. <https://doi.org/10.1016/j.jechem.2018.03.010>.
- [47] P. Lazar, R. Mach, M. Otyepka, Spectroscopic Fingerprints of Graphitic, Pyrrolic, Pyridinic, and Chemisorbed Nitrogen in N-Doped Graphene, J. Phys. Chem. C. 123 (2019) 10695–10702. <https://doi.org/10.1021/acs.jpcc.9b02163>.
- [48] A.H.M. Al-antaki, T.M.D. Alharbi, S. Kellici, N.P. Power, W. Lawrance, C.L. Raston, Vortex Fluidic

- Mediated Synthesis of TiO<sub>2</sub> Nanoparticle/MXene Composites, *ChemNanoMat*. 6 (2020) 657–662.  
<https://doi.org/10.1002/cnma.201900779>.
- [49] R.D. Bonetto, P.E. Zalba, M.S. Conconi, M. Manassero, The Rietveld Method Applied to Quantitative Phase Analysis of Minerals Containing Disordered Structures, *Rev. Geológica Chile*. 30 (2003) 103–115. <https://doi.org/10.4067/S0716-02082003000100007>.
- [50] R.B. Rakhi, B. Ahmed, M.N. Hedhili, D.H. Anjum, H.N. Alshareef, Effect of Postetch Annealing Gas Composition on the Structural and Electrochemical Properties of Ti<sub>2</sub>CT<sub>x</sub> MXene Electrodes for Supercapacitor Applications, *Chem. Mater.* 27 (2015) 5314–5323.  
<https://doi.org/10.1021/acs.chemmater.5b01623>.
- [51] C.H. Sun, X.H. Yang, J.S. Chen, Z. Li, X.W. Lou, C. Li, S.C. Smith, G.Q. Lu, H.G. Yang, Higher Charge/Discharge Rates of Lithium-Ions Across Engineered TiO<sub>2</sub> Surfaces Leads to Enhanced Battery Performance, *Chem. Commun.* 46 (2010) 6129–6131. <https://doi.org/10.1039/c0cc00832j>.
- [52] X. Yang, Y. Yang, H. Hou, Y. Zhang, L. Fang, J. Chen, X. Ji, Size-Tunable Single-Crystalline Anatase TiO<sub>2</sub> Cubes as Anode Materials for Lithium Ion Batteries, *J. Phys. Chem. C*. 119 (2015) 3923–3930.  
<https://doi.org/10.1021/jp512289g>.
- [53] L. Sun, W. Liu, R. Wu, Y. Cui, Y. Zhang, Y. Du, S. Liu, S. Liu, H. Wang, Bio-Derived Yellow Porous TiO<sub>2</sub>: The Lithiation Induced Activation of an Oxygen-Vacancy Dominated TiO<sub>2</sub> Lattice Evoking a Large Boost in Lithium Storage Performance, *Nanoscale*. 12 (2020) 746–754.  
<https://doi.org/10.1039/c9nr09042h>.
- [54] Y. Wang, S. Duan, Z. Tian, Y. Shen, M. Xie, X. Guo, X. Guo, Fabrication of TiO<sub>2</sub>@Carbon Core-Shell Nanosheets for Advanced Lithium-Ion Batteries with Excellent Cyclability, *J. Mater. Chem. A*. 5 (2017) 6047–6051. <https://doi.org/10.1039/c6ta11187d>.
- [55] M. Mao, F. Yan, C. Cui, J. Ma, M. Zhang, T. Wang, C. Wang, Pipe-Wire TiO<sub>2</sub>-Sn@Carbon Nanofibers Paper Anodes for Lithium and Sodium Ion Batteries, *Nano Lett.* 17 (2017) 3830–3836.  
<https://doi.org/10.1021/acs.nanolett.7b01152>.
- [56] C. Yang, Y. Liu, X. Sun, Y. Zhang, L. Hou, Q. Zhang, C. Yuan, In-situ Construction of Hierarchical Accordion-Like TiO<sub>2</sub>/Ti<sub>3</sub>C<sub>2</sub> Nanohybrid as Anode Material for Lithium and Sodium Ion Batteries, *Electrochim. Acta*. 271 (2018) 165–172. <https://doi.org/10.1016/j.electacta.2018.03.118>.
- [57] C. (John) Zhang, S.J. Kim, M. Ghidui, M.Q. Zhao, M.W. Barsoum, V. Nicolosi, Y. Gogotsi, Layered Orthorhombic Nb<sub>2</sub>O<sub>5</sub>@Nb<sub>4</sub>C<sub>3</sub>T<sub>x</sub> and TiO<sub>2</sub>@Ti<sub>3</sub>C<sub>2</sub>T<sub>x</sub> Hierarchical Composites for High Performance Li-ion Batteries, *Adv. Funct. Mater.* 26 (2016) 4143–4151. <https://doi.org/10.1002/adfm.201600682>.
- [58] L. Li, G. Jiang, C. An, Z. Xie, Y. Wang, L. Jiao, H. Yuan, Hierarchical Ti<sub>3</sub>C<sub>2</sub>@TiO<sub>2</sub> MXene hybrids with

## Supporting Information

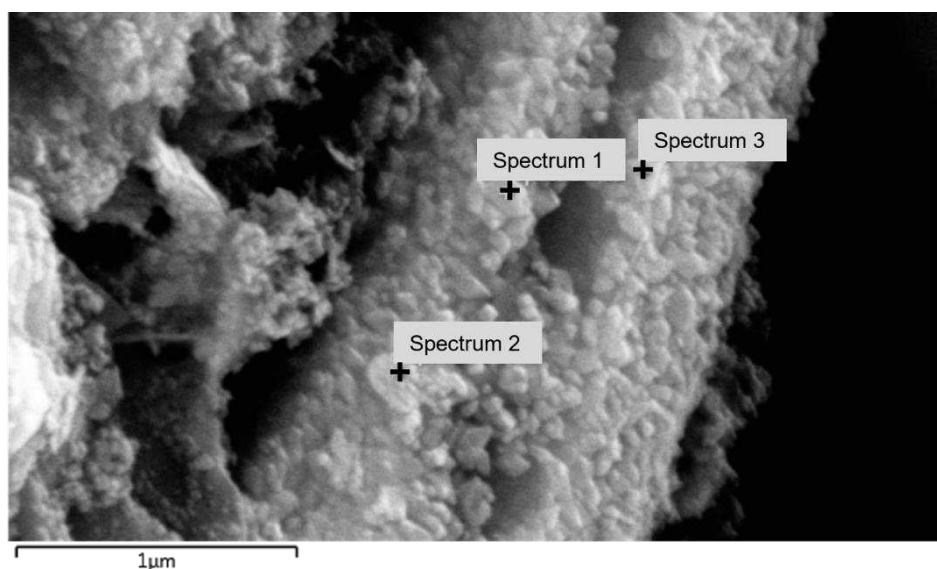


**Fig. S1.** Electron image showing EDS of  $\text{TiO}_2$  particles on the surface of NMT nanocomposites.

**Table S1.** elemental compositions of the surface of NMT nanocomposites.

TiO <sub>2</sub> particle							
Spectrum Label (+)	C	N	O	F	Al	Ti	Total
Spectrum 1	0	0	20.75	0	0.85	78.41	100
Spectrum 2	0	0	26.52	0	0.71	72.76	100
Spectrum 3	0	0	20.81	0	1.25	77.94	100
Statistic							
Max	0	0	26.52	0	1.25	78.41	
Min	0	0	20.75	0	0.71	72.76	
Average	0	0	22.69	0	0.94	76.37	
Standard Deviation	0	0	3.32	0	0.28	3.13	

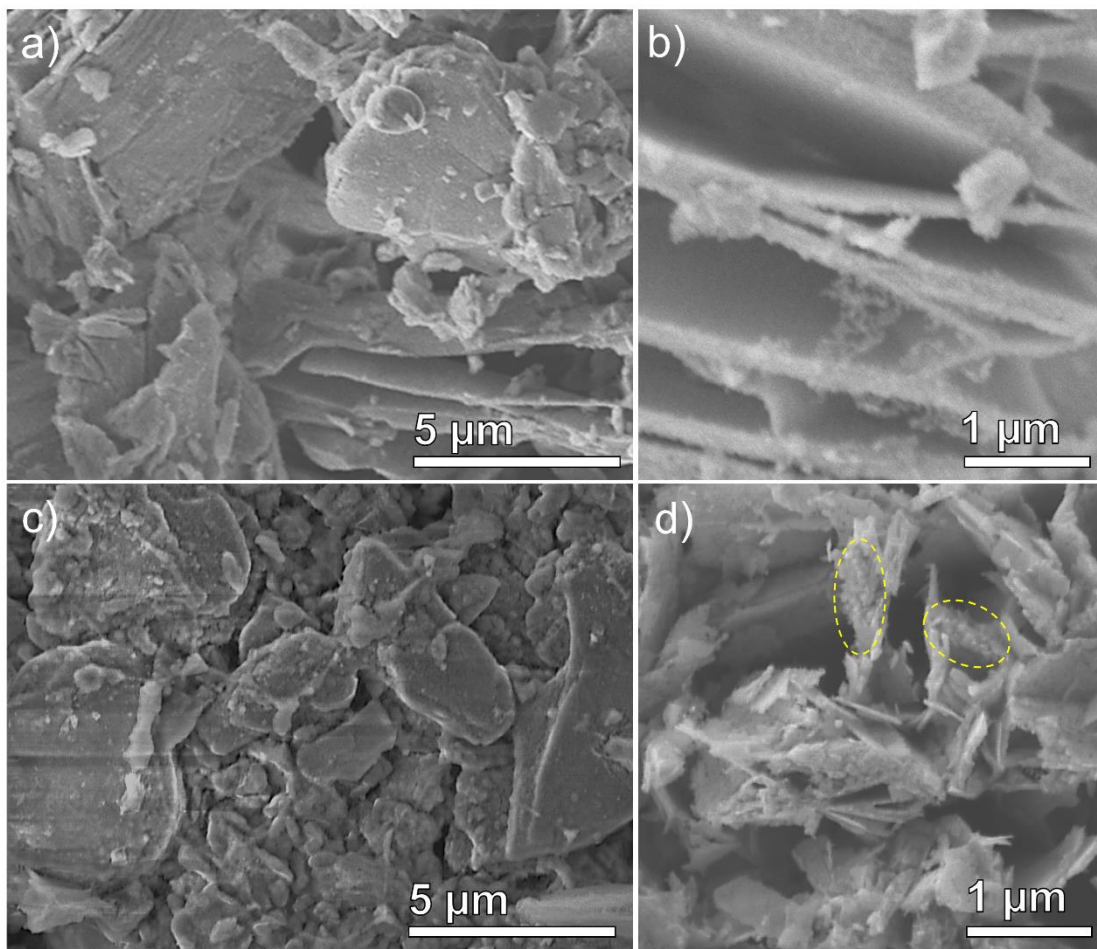


**Fig. S2.** SEM imaging of NMT anode before (a-b) and after (c-d) 100 cycles. Yellow dotted circles in (d) indicate presence of  $\text{TiO}_2$  nanoparticles.

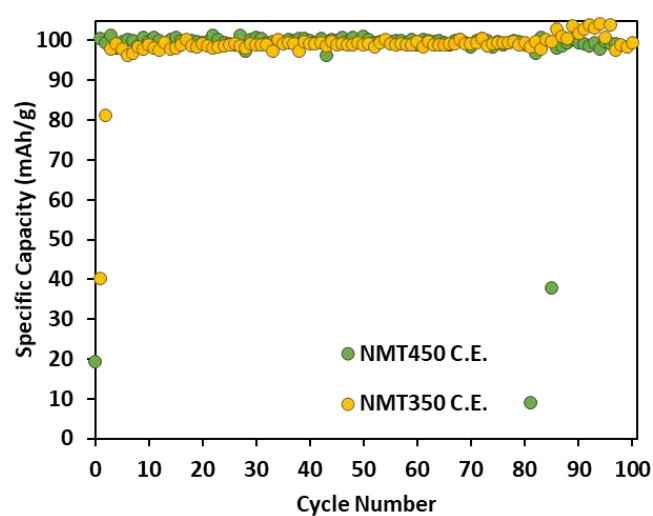


**Fig. S3.** Coulombic efficiencies of the NMT350 and NMT450 electrodes when galvanostatically cycled using a current density of 30 mA/g in the potential region of 0 – 3 V.

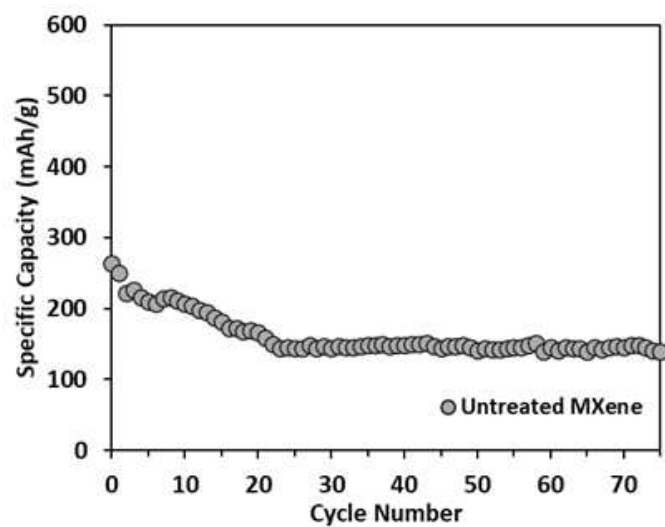


**Fig. S4.** Specific discharge capacities of the untreated MXene electrode using a current density of 30 mA/g in the potential region of 0 – 3 V.

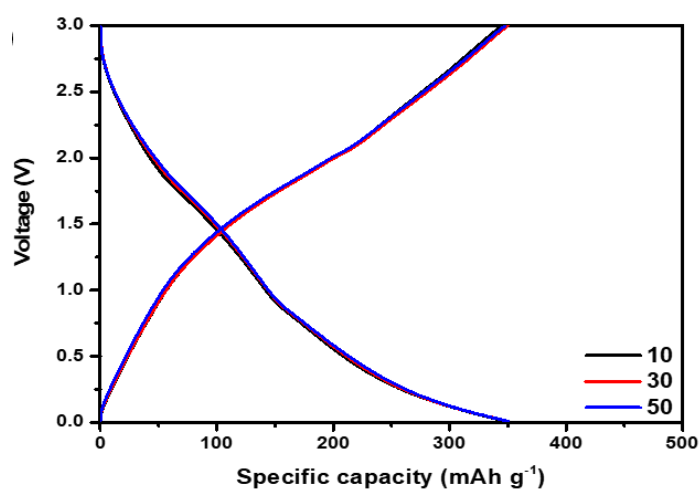


**Fig. S5.** Voltage profiles of the 10th, 30th and 50th cycles of the NMT450 electrode cycled using a current density of 30 mA/g in the potential region of 0 – 3 V.

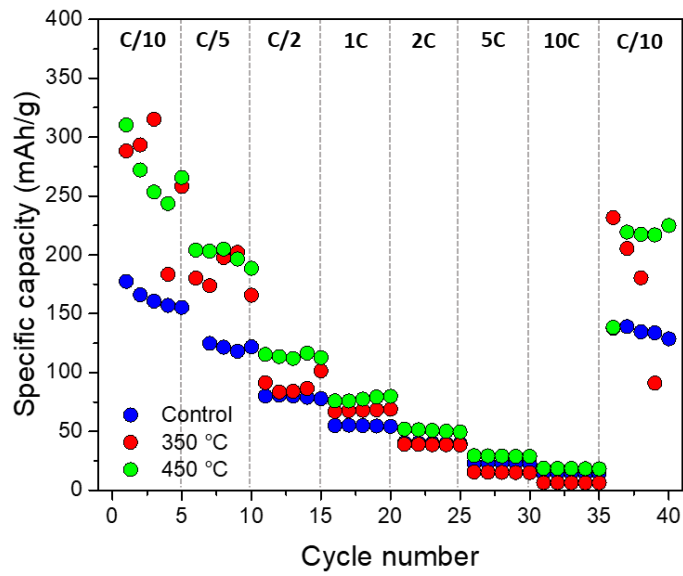


**Fig. S6.** Rate capability testing for the untreated MXene control, NMT350 and NMT450 electrodes showing the specific discharge capacity.